



Studying the Impact of Radioactive Charging on the Microphysical Evolution and Transport of Radioactive Aerosols with the TOMAS-RC v1 framework

Petros Vasilakos¹, Yong-Ha Kim², Jeffrey R. Pierce³, Sotira Yiacoumi², Costas Tsouris^{2,4}, and Athanasios Nenes^{1,5,6,7,†}

¹ School of Chemical and Biomolecular Engineering, Georgia Institute of Technology, Atlanta, Georgia, 30332, USA

² School of Civil and Environmental Engineering, Georgia Institute of Technology, Atlanta, Georgia, 30332, USA

³ Department of Atmospheric Science, Colorado State University, Fort Collins, CO, 80524, USA

⁴ Oak Ridge National Laboratory, Oak Ridge, Tennessee, 37831-6181, USA

⁵ School of Earth and Atmospheric Sciences, Georgia Institute of Technology, Atlanta, Georgia, 30332, USA

⁶ Foundation for Research and Technology-Hellas, Patras, GR 26504, Greece

⁷ National Observatory of Athens, Palea Penteli, GR 15236, Greece

1 †Corresponding Author: A. Nenes (athanasios.nenes@gatech.edu)

2

3

4

5

6

7



Abstract

Radioactive charging can significantly impact the way radioactive aerosols behave, and as a result their lifetime, but such effects are neglected in predictive model studies of radioactive plumes. The objective of this work is to determine the influence of radioactive charging on the vertical transport of radioactive aerosols in the atmosphere, through its effect on coagulation and deposition, as well as quantifying the impact of this charging on aerosol lifetime. The Two-Moment Aerosol Sectional (TOMAS) microphysical model was extended to account for radioactive charging effects on coagulation in a computationally efficient way. The expanded model, TOMAS-RC (TOMAS with Radioactive Charging effects), was then used to simulate the microphysical evolution and deposition of radioactive aerosol (containing the isotopes ^{131}I and ^{137}Cs) in a number of idealized atmospheric transport experiments. Results indicate that radioactive charging can facilitate or suppress coagulation of radioactive aerosols, thus influencing the deposition patterns and total amount of radioactive aerosol mass available for long-range transport. Sensitivity simulations to uncertain parameters affirm the potential importance of radioactive charging effects. An important finding is that charging of neutral, coarse mode aerosol from background radiation can reduce coagulation rates and extend its lifetime in the atmosphere by up to a factor of 2.

Keywords

Radioactive charging, coagulation, nuclear plant accidents, deposition, aerosol lifetime

Key points:

Radioactive charging can significantly affect the coagulation rate and atmospheric transport of radioactive aerosols.

An increase of particle concentrations remaining in the atmosphere after 5 days up to a factor of 30 was simulated for iodine, and up to a factor of 3 for cesium.



9 1. Introduction

10 Human activities and events can release large amounts of radioactive particles into the
11 atmosphere; nuclear reactor meltdowns such as the Fukushima and Chernobyl accidents, weapon
12 tests, radioactive waste treatment, as well as coal fired power plants constitute important sources
13 of airborne radionuclides (Chesser et al., 2004; Lujaniene et al., 2007; Yoshida & Kanda, 2012;
14 McBride et al., 1977; Mulpuru et al., 1992). The impacts of this radioactivity on the environment
15 and human health depends largely on where it deposits, and underscores the need for its accurate
16 prediction for policy and first response efforts to accidents and other release events.

17 Aerosols carrying radionuclides can spontaneously accumulate electrostatic charge, which
18 affects their microphysical evolution in the atmosphere. Because of this, radioactive aerosol can
19 exhibit a distinctly different behavior when compared to non-radioactive (and neutral) aerosol
20 (Simons, 1981; Clement et al., 1995; Clement & Harrison, 1992; Harrison & Carslaw, 2003; Kim
21 et al., 2014, 2015, 2016). Considering charging effects of radioactive aerosol, immediately impacts
22 their initial deposition patterns. Secondary resuspension and redistribution mechanisms from wild
23 fires, dust events and water runoff downwind of nuclear accidents (Lujanienė et al., 2007; Adeyini
24 & Oladiran, 2007; Yoshenko et al., 2006; Yoshenko et al. 2006; Masson et al., 2011), all contribute
25 to the long-term impacts of release events and are affected by where the primary deposition of
26 radionuclides occur. For example, extensive forest fires between May and August of 1992 in the
27 30-km ring surrounding the Chernobyl-exclusion zone are known to have emitted radioactive
28 aerosols to the atmosphere, detectable at considerable distances (Lujanienė et al., 2007; Ooe et al.,
29 1988). As a result, important secondary contamination was found in areas that were initially not
30 contaminated by radioactivity. The remobilized radionuclides deposited after wild fires were more
31 concentrated and water-soluble, and therefore easily redistributable by water runoff into
32 subsurface water systems (Lujanienė et al., 2007; Yoshenko et al., 2006).

33 Charging of radioactive aerosols occurs from the decay of radionuclides, which can be in
34 either the form of α or β emission (Clement & Harrison, 1992). For alpha emission, an alpha
35 particle of a charge of +2 is ejected from the aerosol, leaving a residual charge of -2. Nevertheless,
36 in general, radioactive aerosols undergoing alpha decay become positively charged because alpha
37 particles can cause significant ionization within the aerosols, which leads to the emission of
38 secondary electrons. In β -decay, the emission of energetic electrons results in a residual charge of
39 +1. These ions ejected to the gas phase can combine with surrounding gas molecules or other



40 aerosols through collision/adsorption. Negative ions produced from ionizing radiation tend to
41 exhibit a higher mobility than positive ions produced (Gunn, 1954; Mohnen, 1976); this
42 asymmetry in mobility leads to the charging of aerosols through the diffusion of ions onto their
43 surface, with a surplus of negative gas-phase ions over positively charged ions. Ion mobilities are
44 dependent upon the molecular weight, temperature and pressure of the surrounding gas (Harrison
45 & Carslaw, 2003; Mohnen, 1976; Clement & Harrison, 1992). Therefore, variability of these
46 factors can lead to a range of mobilities, and charging (Clement & Harrison, 1992). The direct
47 ionization of particles from radioactive decay is called “self-charging”, while collision/adsorption
48 of gas-phase ions generated by the radioactive decay is called “diffusion charging” (Harrison &
49 Carslaw, 2003; Clement et al., 1995; Clement & Harrison, 1992; Kim et al., 2014, 2015, 2016).

50 Because radioactive aerosols can be easily discharged by ionizing radiation (Greenfield,
51 1956), as well as neutralized by ions produced in the containment atmosphere and ion-ion
52 recombination (Clement et al., 1995; Clement & Harrison, 1992), the effects of electrostatic
53 interactions on microphysical processes of aerosols have been frequently neglected (e.g.,
54 Greenfield, 1957). However, many radioactive aerosols can be appreciably charged in open air
55 (Kim et al., 2015), suggesting that several microphysical processes of the aerosols can be affected
56 by radioactive charging causing electrostatic interactions (e.g., coagulation (Clement et al., 1995;
57 Kim et al., 2014, 2016) and impacting the rate of wet scavenging (Tripathi and Harrison, 2001;
58 Sow and Lemaitre, 2017). Chemical transport models (CTMs) with explicit aerosol microphysics
59 are well-posed to consider all the relevant processes that control the transport and deposition of
60 radioactive aerosol (e.g., condensation/evaporation of semi-volatile species, coagulation of
61 particles, cloud processing, wet/dry deposition and horizontal/vertical transport). State-of-the-art
62 atmospheric models, however, do not account for radioactivity impacts on aerosol microphysics
63 (e.g., Yoshenko et al., 2006; Christoudias et al., 2013). This omission introduces an unknown, and
64 potentially important, bias in the predicted deposition patterns following a radioactivity release
65 event.

66 This study is an initial step to develop a comprehensive atmospheric modeling approach to
67 account for the effects of radioactive charging on the microphysical evolution, transport and
68 deposition of radioactive aerosol from the atmosphere. The established Two-Moment Aerosol
69 Sectional (TOMAS) aerosol microphysical model (Adams & Seinfeld, 2002) is used to simulate
70 the microphysical evolution of atmospheric particulate matter, and is augmented to include



71 electrostatic particle-particle interactions in the presence of radioactive charging. The expanded
 72 model, called TOMAS-RC (TOMAS with Radioactive Charging effects) is used to study, with
 73 idealized simulations, situations where charging exerts an important influence on the transport and
 74 deposition of radioactive particles.

75

76 **2.Methods**

77 **2.1 TOMAS aerosol microphysical model**

78 The version of the TOMAS model (Adams & Seinfeld, 2002) used here has a resolution of
 79 30 bins, covering particle sizes from 10 nm to 10 μm . TOMAS accounts for all the relevant
 80 atmospheric processes of nucleation, condensation, coagulation, vertical mixing, cloud processing
 81 and deposition, in order to find the number concentration and size distribution of the modeled
 82 aerosol. For the needs of this study only dry deposition, vertical mixing and coagulation were
 83 active. TOMAS tracks two independent moments, number and mass, of the aerosol size
 84 distribution for each size bin:

$$85 \quad N_k = \int_{x_k}^{x_{k+1}} n_k(x) dx \quad (1)$$

$$86 \quad M_k = \int_{x_k}^{x_{k+1}} x n_k(x) dx \quad (2)$$

87 where N_k, M_k are the total number and mass of aerosol in the k -sized bin, $n_k(x)$ is the number of
 88 particles with masses included between $x + dx$, and x_k is the lowest boundary of the k^{th} bin. The
 89 lowest and the largest boundaries of each cell are defined in terms of dry aerosol mass, in such a
 90 way that the largest boundary has double the mass of the lowest boundary, something that allows
 91 for considerable gains in computational efficiency (Adams & Seinfeld, 2002). A detailed
 92 description of TOMAS is available elsewhere (Adams & Seinfeld, 2002; Lee & Adams, 2012).

93 The aerosol size distributions are influenced by microphysical processes (e.g., deposition,
 94 vertical layer mixing, and coagulation) occurring in each computational cell. The rate of change
 95 for N_k and M_k resulting from coagulation, which is a process modulated by radioactive charging,
 96 are given by (Fuchs, 1964; Tzivion et al., 1987, Adams and Seinfeld, 2002):

$$97 \quad \frac{dN_k}{dt} = 0.5K_{k-1,k-1}N_{k-1}^2 - K_{k,k}N_k^2 - N_k \sum_{i=k+1}^I K_{k,i}N_i + \psi_{k-1} \sum_{i=1}^{k-2} K_{k-1,i}M_i$$

$$- \psi_{k-1} \sum_{i=1}^{k-1} K_{k,i}M_i - \frac{\psi_{k-1} - f_{k-1}}{2x_{k-1}} \xi \sum_{i=1}^{k-1} K_{k,i}M_i m_i - \frac{\psi_{k-1} - f_{k-1}}{2x_{k-1}} \xi \sum_{i=1}^{k-2} K_{k-1,i}M_i m_i \quad (3)$$



$$\begin{aligned}
 \frac{dM_k}{dt} = & K_{k-1,k-1}N_{k-1}M_{k-1} - K_{k,k}N_kM_k + N_k \sum_{i=1}^{k-1} K_{k,i}M_i - M_k \sum_{i=k+1}^I K_{k,i}N_i \\
 98 \quad & + \psi_{k-1}x_k \sum_{i=1}^{k-2} K_{k-1,i}M_i - \psi_k x_{k+1} \sum_{i=1}^{k-1} K_{k,i}M_i + \frac{f_{k-1}}{2} \xi \sum_{i=1}^{k-2} K_{k-1,i}M_i m_i \\
 & - \frac{f_k}{2} \xi \sum_{i=1}^{k-1} K_{k,i}M_i m_i + \frac{\psi_{k-f_k}}{2x_k} \xi^3 \sum_{i=1}^{k-1} K_{k,i}M_i m_i^2 - \frac{\psi_{k-1-f_{k-1}}}{2x_{k-1}} \xi^3 \sum_{i=1}^{k-2} K_{k-1,i}M_i m_i^2
 \end{aligned} \quad (4)$$

99 where i and k represent the size bins between which coagulation takes place, $K_{k,i}$ is the coagulation
 100 coefficient between these two bins, I is the total number of size bins which is equal to 30 for this
 101 case, ψ and f are weighting factors described in Tzivion et al. 1987, ξ is the closure parameter
 102 determined size range of each bin (here, $\xi = 1.0625$), x is the lowest dry mass boundary of the cell,
 103 m_i is the average particle mass in bin i , and t is the time.

104 In Eqs. (3) and (4), the coagulation coefficient, K , is the parameter controlling the
 105 coagulation rate of aerosols, and it can be affected by several collision mechanisms involving
 106 interparticle forces and flow regimes (Seinfeld and Pandis, 2006). In TOMAS, it is assumed that
 107 Brownian motion is the dominant collision mechanism (Adams & Seinfeld, 2002; Lee & Adams,
 108 2012). In TOMAS-RC, the Brownian coagulation coefficient is augmented to include the effects
 109 of radioactive charging, following the suggestions of Clement et al. (1995); Kim et al. (2016), and
 110 as described below.

111 2.2 Coagulation of radioactive aerosols

112 Charging effects on the coagulation rate between particles i and k are introduced through a
 113 “correction factor” multiplier, $\bar{W}_{k,i}$, applied to the Brownian coagulation kernel at each aerosol
 114 microphysical step (Fig. 1). $\bar{W}_{k,i}$ in TOMAS-RC is based on the “stability function” correction
 115 factor formulation (Spellman, 1970; Seinfeld & Pandis, 2006):

$$116 \quad W_{k,i} = \frac{\gamma}{e^{\gamma} - 1} \quad (5)$$

117 with $\gamma = \frac{j_k j_i e^2}{4\pi\epsilon_0\epsilon(r_k+r_i)k_B T}$, j_k, j_i are the charges of particle k and i respectively, e is the elementary
 118 electrical charge, ϵ_0 is the electrical permittivity of vacuum and ϵ is the dielectric constant of air.
 119 Also, r_k and r_i are the radii of aerosol particles k and i , respectively, k_B is the Boltzmann constant,
 120 and T is the temperature. $W_{k,i}$ is applied as an enhancement factor to the Brownian kernel; as the
 121 charge of either the colliding particles approaches zero (i.e., $j_k j_i \rightarrow 0$), $\gamma \rightarrow 0$ and $W_{k,i} \rightarrow 1$ (because
 122 $e^{\gamma} \sim 1 + \gamma$ for small γ) coagulation approaches that expected from Brownian diffusion of neutral
 123 particles. This limit is relevant for the coagulation between small particles that typically carry an



124 average charge of less than 1 ($\gamma < 0.1$), and subsequently their coagulation is not impacted by
 125 charging effects. In the case of particles with opposite sign charges, $\gamma < 0$ and $W_{k,i} > 1$ meaning that
 126 coagulation is enhanced; for particles with like charges, $\gamma > 0$ and $W_{k,i} < 1$ leading to inhibition of
 127 coagulation.

128 Equation (5) depends strongly on the number of charges existing on the coagulating
 129 particles. An appropriate theory is therefore required to calculate at each coagulation timestep (Fig.
 130 1) the number of charges that develop on the aerosol population. In the presence of self-charging
 131 and diffusion charging, a Gaussian distribution can be used to describe the charge distribution that
 132 develops for particles in each size bin k (Clement et al., 1995; Gensdarmes et al., 2001; Kim et al.,
 133 2016):

$$134 \frac{N_{kj}}{N_k} = \frac{1}{\sqrt{2\pi}\sigma_k} \exp\left(-\frac{(j-\bar{J}_k)^2}{2\sigma_k^2}\right) \quad (6)$$

135 where N_{kj} is the number concentration (m^{-3}) of aerosols in size bin k carrying charge j . N_k is the
 136 total number of particles in bin k ($N_k = \sum_j N_{kj}$) and \bar{J}_k , σ_k are the mean aerosol charge and standard
 137 deviation of the aerosol charge distribution for size bin k , given by:

$$138 \sigma_k^2 = y_k + \frac{1}{2\omega_k}, \quad \bar{J}_k = \begin{cases} y_k - \left(\frac{y_k(X-1)}{\exp(2\omega_k y_k - 1)}\right) & \omega_k y_k > 0.22 \\ y_k + \frac{X-1}{2\omega_k} & \omega_k y_k \leq 0.22 \end{cases}, \quad y_k = \frac{\varepsilon_0 \eta_k}{e\mu_- n_0},$$

139 where $\omega_k = \frac{e^2}{8\pi\varepsilon_0 r_k k_b T}$ is a parameter describing the effects of diffusion charging, $X = \frac{\mu_+}{\mu_-}$ is the
 140 asymmetry/mobility ratio, μ_+ and μ_- are the mobilities of positive and negative ions, respectively
 141 ($\text{m}^2 \text{V}^{-1} \text{s}^{-1}$), y_k is the positive charge accumulated via self-charging and n_0 is the total number of
 142 ions in the air. The size-dependent radioactive decay per particle (η_k), in each size bin, required to
 143 obtain y_k is determined from the specific radioactive decay rate η_0 for each species (Clement &
 144 Harrison, 1992):

$$145 \eta_k = \eta_0 r_k^3 \quad (7)$$

146 Calculation of y_k also requires the total number n_0 of ions (positive and negative) produced
 147 from natural radioactivity, cosmic rays, and decay of radionuclides attached to aerosols and is
 148 given by (Clement et al., 1995; Harrison & Carslaw, 2003):



$$149 \quad n_0 = \sqrt{\frac{q_b + q_I}{\alpha_{rc}}}, \quad (8)$$

150 where q_b is the rate of ionization by radon and cosmic radiation, q_I is the rate of ionization caused
 151 by radioactive aerosols, and α_{rc} is the rate coefficient of ion-ion recombination.

152 Equation 6 applies to background aerosols as well; in this case $\eta_{\kappa} \rightarrow 0$ so $y_k \rightarrow 0$). The
 153 resulting distribution has an average charge, $\bar{J}_k = \frac{X-1}{2\omega_k}$, that represents the effects of diffusion
 154 charging acquired by particles from background radiation, and has been validated in a number of
 155 studies (e.g., Gensdarmes et al., 2001; Kim et al., 2014; Kim et al., 2016).

156 The size and charge are important variables in Eqs. (5), (6) and (7) and continuously vary
 157 over the whole size distribution. A singular charge distribution ($\bar{J}_k = y_k$, Eq. (6)), reduces to the
 158 symmetrical Boltzmann distribution which occurs as the ion asymmetry ratio X approaches 1. The
 159 mean charge of each aerosol size bin can then be used to approximately calculate the correction
 160 factor. For lower values of X however, the resulting charge distributions are asymmetric and not
 161 well approximated by the Boltzmann distribution due to the higher mobility of the negative ions
 162 (Clement & Harrison, 1992), making the average charge an insufficient proxy for the correction
 163 factor. To overcome this limitation, the average correction factor $\bar{W}_{k,i}$ proposed by Clement et al.
 164 (1995) and validated by Kim et al. (2016), which can consider the interaction of all charged
 165 aerosols, was employed.

$$166 \quad \bar{W}_{k,i} = 1 + \frac{\sum_{l \neq 0}^{\infty} N_{k,l} N_{i,l} (W_{k,l}^{-1} - 1)}{\sum_{l=0}^{\infty} N_{k,l} \sum_{l=0}^{\infty} N_{i,l}} \quad (9)$$

167 If repulsive electrostatic forces are predominant among aerosols, the sign of the fractional
 168 term in the right-hand side of Eq. (9) is changed to minus and the average correction factor is less
 169 than unity (i.e. radioactive charging inhibits coagulation). Radioactive charging impacts in
 170 TOMAS-RC are introduced by multiplying the Brownian coagulation coefficient by $\bar{W}_{k,i}$ (Fig. 1).

171 2.3 Optimization of Coagulation Corrections for Broad Charge Distributions

172 During simulations, the width of the charge distribution for each bin, approximated by $\bar{J}_k \pm$
 173 $5\sigma_k$, is proposed Kim et al., (2016) to determine the summations in Eq. (9). The larger the average
 174 charge and the deviation of the distribution for that bin, the larger the summation index $l = \bar{J}_k \pm$
 175 $5\sigma_k$ of Eq. (9) becomes, which, in the case of large particles carrying significant charges (Clement



176 et al., 1995; Clement & Harrison, 1992; Kim et al., 2013) can lead to values of l of the order 10^3 .
 177 The computational burden in such situations quickly becomes overwhelming, as the required
 178 calculations for the correction factor scale with $k^2 l^2$ at each microphysical TOMAS-RC timestep
 179 (because the summations of Eq. (9) need to be recalculated every time to consider all interactions
 180 between all size bins k , as well as every possible charge value for bin l). In the case of radioactive
 181 particles with a diameter greater than $2 \mu\text{m}$, the average charge attained can be, depending on the
 182 radionuclide of question, on the order of thousands, which increases the computation time by at
 183 least 10^4 when compared to smaller particles with \bar{J}_k values less than 10. The computational burden
 184 is further increased by broadening of the charge distribution – which expands the summation in
 185 Eq. (9) to include substantially more terms.

186 To accelerate calculations while minimizing loss in accuracy, instead of iterating over all
 187 possible values of l for each size bin, iterations are done over a limited charge interval about the
 188 mean $[\bar{J}_k - 2\sigma_k, \bar{J}_k + 2\sigma_k]$, which for the normal charge distribution encompasses 95% of the
 189 possible charge values. Other values for the intervals were tested, spanning from $\bar{J}_k \pm 5\sigma_k$ to $\bar{J}_k \pm$
 190 σ_k and the results showed the best agreement with the lowest associated computational cost for
 191 $[\bar{J}_k - 2\sigma_k, \bar{J}_k + 2\sigma_k]$. We additionally employ an adaptive, linearly increasing, step for the iterator
 192 j of Eq. (8), which was used when the average charge exceeded 100. This step was derived
 193 empirically based on simulation results for the cases where \bar{J}_k and σ_k were highest, by determining
 194 the limiting case from all the simulation scenarios, which occurred for ^{131}I when the particle size
 195 and concentrations were maximum. We find that using a step of $\Delta n_k = \frac{|4\sigma_k|}{100} + 1$ (where Δn_k is the
 196 step size for a given particle size r_k , σ_k is the deviation of the charge distribution for size bin k)
 197 considerably accelerates the calculations at a minimal loss of computational accuracy.

198 Figure 2 shows the comparison between the approach described in Clement et al. 1995 and
 199 the aforementioned scheme, showing the average enhancement factors between particles of a given
 200 size r_k , as a function of a coagulating particle with size, r_i . For particles with r_k values of less than
 201 $0.345 \mu\text{m}$, coagulation tends to be unaffected for smaller sizes and enhanced for larger ones, since
 202 particles of that size carry a very small negative charge of less than -1. As small charge means that
 203 their coagulation with other small particles is not inhibited, while enhancement is seen for larger
 204 sized particles carrying a large positive charge ($\bar{J}_k > 100$). For particles with r_k values of 0.801
 205 μm ($\bar{J}_k \sim 2$), there is an initial enhancement between the negatively charged, small-sized part of the
 206 distribution, an inhibition for mid-sized, positively charged particles, and a subsequent



207 enhancement for the larger, strongly positive particles. Since these particles carry the same sign
208 charge, this enhancement can only be explained by a considerably negatively charged tail of the
209 charge distribution ($\sigma_k = 3.71$) of the particles with $r_k=0.801 \mu\text{m}$, which shows that the average
210 charge is not a good predictor of radioactive coagulation, and the use of a distribution is necessary.
211 For the larger particles with $r_k=1.6 \mu\text{m}$ ($\bar{J}_k \sim 21.5$), there is an initial expected enhancement of
212 coagulation between them and the negatively charged smaller particles, and a strong inhibition for
213 the positively charged larger particles.

214 Using the optimizations described above, calculation of $\bar{W}_{k,i}$ in TOMAS-RC is accelerated
215 by up to 3 orders of magnitude. When compared to using the exact summation calculations over a
216 charging distribution that considers $\pm 5 \sigma$ about the mean \bar{J}_k , there is no apparent loss in accuracy,
217 as the enhancement factors computed for coagulation of ^{137}Cs aerosol (Fig. 2) are similar to the
218 ones reported by Clement et al. (1995).

219

220 **2.5 Atmospheric simulation scenarios**

221 To demonstrate the capabilities of TOMAS-RC, it is used to simulate the deposition of
222 ^{137}Cs and ^{131}I during an idealized radionuclide release incident. Simulation results for neutral
223 background aerosol are obtained under the same initial conditions and given for reference. The
224 specific radionuclides are considered, as they have been released during nuclear plant accidents
225 (Mason et al., 2011; Yoshida & Kanda, 2012; Kauppinen et al., 1986). The characteristics of the
226 idealized simulations are provided in Table 1. Values for radioactivity pertinent parameters were
227 obtained from previous studies (Clement & Harrison, 1992; Clement et al., 1995; Kim et al., 2015).
228 The height of the top layer was set to 1 km so that it could capture a potential plume from a nuclear
229 accident (Chesser et al., 2004).

230 For all simulations considered, three aerosol microphysical processes were accounted for
231 i.e., coagulation, vertical mixing (turbulent diffusion) and dry deposition (Fig. 1) – as a means of
232 carrying out a semi-Lagrangian simulation, where an air mass is tracked as it advected away from
233 its release point, but still allowed to vertically mix. Such a simulation resolves the processes that
234 impact the microphysical evolution of the aerosols contained within the column and also can be
235 used to compute the depositional loss of radioactive. The simulation duration is set to 5 days,
236 which covers most of the lifetime of tropospheric aerosol (Seinfeld & Pandis, 2006). We assume
237 that η_0 of the radioactive aerosol is constant throughout the simulation. The effects of radioactive



238 charging were assessed by examining the aerosol fields with and without radioactivity effects and
239 for four different values of the ion mobility ratio (X): 0.7, 0.8, 0.9 and 1, for each radionuclide
240 considered. In all simulations, it was assumed that each of the five vertical levels had an initial
241 particle population that followed a log-normal distribution with a single mode. Dry deposition was
242 the only active mechanism of aerosol loss from the atmospheric column.

243 The microphysical characteristics of the radioactive aerosol emissions are highly uncertain,
244 so we assess the importance of radioactive charging for a wide range of initial distributions, by
245 varying the geometric mean diameter, D_g , initial concentration of particles, N_0 , and the geometric
246 standard deviation σ_g of the radioactive aerosol. The range of values used for this study is shown
247 in Table 2. The results of the sensitivity analysis were evaluated using the column integrated mass
248 ratio (CIMR) of aerosol remaining in the column:

$$249 \quad CIMR = \frac{MR_t}{MNR_t} \quad (10)$$

250 where MR_t and MNR_t are the total amounts of mass residing in the column after time t for the
251 radioactive and nonradioactive cases, respectively.

252 3. Results

253 Deposition characteristics of radioactive aerosols in the column consisting of five vertical
254 layers were investigated using the TOMAS model with and without the average correction factor
255 (hereafter radioactive and nonradioactive cases, respectively). The column spanned altitudes from
256 0 to 1000 m with a resolution of 200 m, with each layer having the same amount of initial
257 radionuclide mass. Coagulation characteristics of radioactive aerosols in one layer were
258 investigated first before analyzing the vertical transport and deposition of the aerosols. Then the
259 aerosol size distribution and total mass residing in each layer were analyzed to elucidate the effects
260 of the radioactive charging on the deposition of radioactive aerosols.

261 3.1 Aerosol Size Distributions

262 Figure 3 presents the microphysical evolution, expressed as changes in the size distribution,
263 of ^{137}Cs aerosols at 400-m altitude over time. The initial size distributions were selected so that a
264 significant number of large particles were present, leading to an appreciable impact of radioactive
265 charging. Shown are the changes that would occur in the presence (solid lines) and absence (dashed



266 lines) of radioactive charging. In the presence of charging effects, ^{137}Cs aerosols coagulate more
267 slowly than nonradioactive aerosols. This behavior can be seen in a less dramatic shift of the modal
268 peak towards larger aerosol sizes over time when charges are present (Fig. 3). Slowing of
269 coagulation occurs because negative ions in the atmosphere diffuse more quickly toward the
270 aerosol surfaces (i.e., $X < 1$), so most aerosol acquires a net negative charge (Fig. 4a). Since many
271 particles smaller than $0.8\ \mu\text{m}$ are not charged (Fig. 4a), their coagulation is almost unaffected
272 between neglecting and considering charging effects, while particles between 0.8 and $5\ \mu\text{m}$ exhibit
273 the most dramatic inhibition (Fig. 3), since these are the particles that accumulate the largest
274 amount of negative charges (Fig. 4a). Particles larger than $5\ \mu\text{m}$ carry even larger amounts of
275 negative charge, but are not present in significant concentrations ($d_g = 1.5\ \mu\text{m}$) to affect the shape
276 of the number distribution (Fig. 3).

277 The evolution of the size distributions of ^{131}I aerosols at 400-m altitude is presented in Fig.
278 5. Similarly to ^{137}Cs , particles below $4\ \mu\text{m}$ are negatively charged, inhibiting their coagulation.
279 Even for a low value of X (0.7) however, all particles above $4\ \mu\text{m}$ are positively charged (Fig. 4b),
280 which leads to notable differences in the predicted distributions when neglecting and considering
281 charging effects. Particles up to $1.3\ \mu\text{m}$ in diameter are slightly more negatively charged than ^{137}Cs ,
282 and the coagulation between those particles and the positively charged larger bins with a diameter
283 of $5\ \mu\text{m}$ and above is significantly enhanced leading to reduced predicted number concentrations
284 of both the large and small particles when compared to assuming Brownian coagulation alone (Fig.
285 5). For particles close to the initial modal diameter of $1.5\ \mu\text{m}$ (where most of the aerosol number
286 lies), and up to sizes of $3\ \mu\text{m}$, coagulation is strongly inhibited, which is a result of the negative
287 charges these particles carry (Fig. 4b).

288

289 **3.2 Dry deposition fluxes of radionuclides.**

290 Figure 6 shows contour plots of CIMR from Eq. (10), for the ^{137}Cs aerosol simulation after
291 5 days of microphysical evolution, as a function of initial geometric mean diameter and initial
292 concentration. As the geometric mean diameter and total concentration of the initial aerosol size
293 distribution increase, so does the CIMR, indicating that fewer ^{137}Cs aerosols were deposited. This
294 behavior means that the lifetime of the radioactive aerosol increases and particles deposit over a
295 longer distance away from the source. For the more extreme cases, where the concentrations were
296 upwards of $10^{11}\ \text{m}^{-3}$ and the geometric mean diameter was larger than $3\ \mu\text{m}$, the amount of ^{137}Cs



297 aerosols remaining suspended in the atmosphere, and therefore available for transport, was
298 increased by up to 260% (Fig. 6a), compared to the case of neutral coagulation. Increasing particle
299 concentrations for a given initial particle diameter, meant that the number of particles that could
300 carry a larger amount of same charges was increased, even though the average charge is
301 independent of the number concentration, due to the deviation of the charge distribution (Eq. (6)),
302 leading to inhibition. At the same time, increasing the initial particle size for a constant number
303 concentration augments the number of larger particles that are able to sustain a larger number of
304 charges (Figs. 4a, b), which in turn translates to stronger impacts of charging on coagulation.

305 It is important to understand the change in deposition behavior of ^{137}Cs particles as the
306 relative mobility of positive vs. negative particles (i.e., X) changes, especially if the radioactive
307 decay has a range of negative/positive ions produced (certainly the case for diffusion charging in
308 air, where the carrier molecules of ions may be N_2 or O_2 ; Harrison & Carslaw, 2003). For situations
309 where X is less than 0.9 (Figs. 6a, b), the entire particle distribution is negatively charged (Fig. 4a),
310 which leads to a distribution-wide inhibition of coagulation. The inhibition is stronger for the
311 lowest value of $X=0.7$, since the higher mobility of negative ions leads to particles becoming
312 strongly negatively charged which limits their interactions. When $X\sim 1$ (Fig. 6d), particles up to
313 sizes of $3\ \mu\text{m}$ have a mean charge of zero, while larger ones are all positively charged with an
314 average charge increasing exponentially with size (Fig. 4a), meaning that as the concentration of
315 aerosol larger than $3\ \mu\text{m}$ increases, the coagulation between them is suppressed due to the
316 accumulation of large charges of the same sign. In the case of a mobility ratio of less than 0.9 (Figs.
317 6a, b), the charge of all particles is negative leading to strong coagulation inhibition.

318 An interesting behavior is observed on CIMR when X increases from 0.9 to unity (Figs. 6c,
319 d); while the amount of mass deposited is increased with increasing X (Figs. 6a, b), the opposite
320 trend is observed between $X=0.9$ and 1 (Figs. 6c, d), with the mass deposited decreasing with an
321 increase in X . The reason for this behavior is that the mean charge of each bin changes sign and
322 from negative becomes positive, even for the smaller sized bins (Fig. 4a). This change increases
323 the coagulation rates between the smaller, negatively charged particles and the larger positively
324 charged particles, but at the same time, inhibits the coagulation between the same large particles.
325 An explanation can be found by looking at the definition of the average charge of each bin. For all
326 ^{137}Cs cases simulated, $\omega_k y_k < 0.22$ and therefore $\bar{J}_k = y_k + \frac{X-1}{2\omega_k}$ (Eq. (6)). When $X\leq 0.8$, the
327 fractional term is negative and larger than y_k . However, when $X=0.9$ and large enough particle



328 sizes, y_k becomes greater than the negative fractional term, leading to these particles becoming
329 positively charged.

330 Figure 7 shows CIMR for ^{131}I aerosols after 5 days under various initial aerosol size
331 distributions. As with ^{137}Cs , less ^{131}I aerosols were deposited, as the mean diameter or total
332 concentration increased. Because the radioactive decay rate of ^{131}I aerosols is nearly 700 times
333 higher than that of the ^{137}Cs aerosols (Table 1), the impact of charging is much more pronounced
334 and can lead to up to a factor of 30 more mass remaining after 5 days of atmospheric processing
335 (Fig. 7d). Similar behavior to ^{137}Cs was observed, with the average charge of some bins changing
336 sign depending on the mobility ratio (Fig. 4b). However, in stark contrast with the ^{137}Cs
337 simulations for the same conditions, all particle sizes above $5\ \mu\text{m}$ are strongly positively charged
338 regardless of the value of the mobility ratio, with the charge of the largest bins being in excess of
339 a 100. The largest impact of radioactive charging for ^{131}I can be seen in the case of $X=0.9$ and 1.
340 Looking at the average charge of each bin for these cases, reveals that the entire distribution is
341 positively charged (Fig. 4b), which in turn leads to very strong inhibition between all bins, and a
342 resulting 30-fold increase in mass remaining after 5 days, if the emitted particles are of large
343 enough (Figs. 7c, d). The effect is slightly more pronounced for the case of a mobility ratio of 0.9,
344 because the maximum charge attained by the largest particles can be higher than for the case of a
345 mobility ratio of unity (Fig. 4b). For X values of 0.7 and 0.8, bins up to $5\ \mu\text{m}$ carry a negative
346 charge that enhances their coagulation with larger positively charged particles, but the significant
347 positive charges attained by the larger particles (Fig. 4b) still leads to overall inhibition, and
348 subsequently to high CIMRs values (Figs. 7a, b), albeit smaller than the ones predicted when $X \geq 0.8$,
349 due to the aforementioned enhancement.

350 To further determine the impact of possible diffusion charging effects on non-decaying
351 particles, simulations were carried out where the radioactive decay rate of the aerosol population
352 was set to a value of 0. In this case, $\eta_k=0 \rightarrow \omega_k y_k = 0$ and therefore $\bar{J}_k = \frac{X-1}{2\omega_k}$ (Eq. (6)). Diffusion
353 charging can have a significant impact on very coarse aerosol (Gunn, 1954) such as dust and
354 volcanic ash, regardless of its composition. Following the same analysis as with the radioactive
355 particles, the same scenarios were studied and results analyzed using the CIMR. While the impact
356 of diffusion charging on small particles (Fig. 8) is negligible, for very large aerosol and high
357 enough concentrations the impact can be significant, especially in environments where the
358 mobility of negative ions is greater than that of the positive ones ($X < 1$). For such cases, all particles



359 gather large negative charges and enhancement factors of less than unity, which inhibits their
360 coagulation and lead to increased aerosol lifetimes.

361 For all cases described above, the geometric standard deviation of the initial aerosol size
362 distribution, σ_g , was also found to affect CIMR. Larger values of σ_g simultaneously increase the
363 number of small and large particles, which in effect augments both the enhancement and inhibition
364 for all cases. Inhibition tends to be favored, since wider distributions carry a higher number of
365 large particles, which subsequently become a larger portion of the total aerosol mass, given that
366 the mass scales cubically with size. These large particles, tend to carry the largest amount of
367 charges (Figs. 4a, b) and are affected the most by radioactive charging. Therefore, increasing their
368 mass fraction for any value of the mobility ratio, will lead to overall inhibition, and also extend
369 the impact of radioactivity to lower initial particle concentrations and diameters, since even in this
370 case an abundance of large particles will be present.

371 4. Conclusions

372 We present the development of the TOMAS-RC model, an expanded version of the
373 TOMAS microphysics model to explicitly treat the effects of radioactive charging on the
374 microphysical evolution during the transport and deposition of radioactive particles away from an
375 atmospheric source. Electrostatic charges induced by radioactive decay, through the mechanisms
376 of self- and diffusion charging, can magnify or reduce the coagulation rates of radioactive particles
377 by producing attractive or repulsive forces. Effects are introduced as a multiplication factor applied
378 to the Brownian coagulation kernel of TOMAS; explicit treatment of the discretized nature of the
379 size distribution, the charge distribution within each size bin and accelerations of the calculation
380 procedure are discussed in detail.

381 The TOMAS-RC model was applied to study the dispersion and microphysical evolution
382 of radioactive particles within a vertically-dispersing atmosphere, and simulations were carried out
383 for aerosols carrying ^{131}I and ^{137}Cs for a wide range of initial aerosol conditions and ion mobilities.
384 Radioactive charging for both radionuclides was found to often have an important impact on the
385 evolution of the particle size distributions and subsequent dry deposition of radioactive aerosol.
386 The effects increased as the initial size or concentrations of radioactive particles increased, due to
387 different ion concentrations. The ratio of mobilities of the positive ions to the negative ions, X ,
388 was found to also have a very strong effect on the evolution of the particle size distribution and



389 deposited particles, especially for the case of ^{137}Cs particles, where depending on the value of X ,
390 some bins of the aerosol distribution can switch sign and behavior altogether (charging enhancing
391 vs. inhibiting coagulation). It should be noted that the charge signs of ^{137}Cs and ^{131}I aerosols can
392 be opposite because of the different charging mechanisms dominating each case, as shown for the
393 case of particles larger than $5\ \mu\text{m}$ for all X values.

394 Through a series of highly idealized simulations, we have shown that the charging of
395 radioactive aerosols can have an appreciable effect on how particles are deposited, with important
396 implications for predicting dispersal patterns after nuclear accidents. However, it has been
397 assumed that only one type of radionuclide is present. More realistic aerosol may contain external
398 or internal mixtures of radionuclides, with very different microphysical evolution from the ones
399 describe here. For example, if both ^{137}Cs and ^{131}I are present in the same column as externally-
400 mixed aerosol, the coagulation would be highly facilitated and thus the deposition rates of
401 radioactive aerosols should be enhanced. Multigenerational products from the decay of
402 radionuclides during atmospheric transport can create conditions of variable X (dependent on
403 particle size and composition) that can lead to very different depositional patterns as well.
404 Coagulation of externally mixed bins, or condensation/evaporation of semi-volatile radionuclides
405 (e.g. ^{131}I , ^{132}I) can create particles of varying compositions, which in turn translates to different
406 rates of radioactive decay and charging mechanisms. Further decay products of radionuclides (e.g.
407 ^{132}Te to ^{132}I) can shift the balance between diffusion and self-charging, and that behavior can
408 induce significant uncertainties in modeling.

409 Since this study only considers dry deposition, the potential role of radioactive charging on
410 wet scavenging is not considered. However, the potential acceleration of the coagulation between
411 fine particles from charging, could make these particles larger and therefore more effective cloud
412 condensation nuclei (CCN), increasing the efficiency by which they are removed from the
413 atmosphere through wet deposition and warm rain process modulation. Coagulation of
414 radionuclides with larger, charged dust particles which are very efficient ice nuclei (IN) may also
415 affect deposition patterns by promoting cold rain processes. Future and ongoing modeling
416 activities (e.g., Kim et al., 2017) should focus on a full account of all such effects to fully elucidate
417 the impact that radioactive charging effects can have on the transport of radioactivity across the
418 globe.

419



420 **Code and data availability**

421 The TOMAS-RC code, as well as the data, are available upon request.

422

423 **Acknowledgments:** This work was supported by the Defense Threat Reduction Agency under
424 grant number DTRA1-08-10-BRCWMD-BAA. This manuscript has been authored by UT-
425 Battelle, LLC under Contract No. DE-AC05-00OR22725 with the US Department of Energy. The
426 United States Government retains and the publisher, by accepting the article for publication,
427 acknowledges that the United States Government retains a non-exclusive, paid-up, irrevocable,
428 world-wide license to publish or reproduce the published form of this manuscript, or allow others
429 to do so, for United States Government purposes. The Department of Energy will provide public
430 access to these results of federally sponsored research in accordance with the DOE Public Access
431 Plan (<http://energy.gov/downloads/doe-public-access-plan>). AN acknowledges support from a
432 Georgia Power Faculty Scholar Chair, a Cullen-Peck Faculty Fellowship and Johnson Faculty
433 Fellow funds.

434



435 **REFERENCES**

- 436 Adams, P. J., and J. H. Seinfeld, Predicting global aerosol size distributions in general circulation
437 models, *J. Geophys. Res.*, 107(D19), 4370, doi:10.1029/2001JD001010, 2002
- 438 M. O. Adeyini, E. O. Oladiran, Recent results on atmospheric radioactivity at Ibadan,
439 Nigeria, *Radiation Measurements*, 41, 330-336, doi: 10.1016/j.radmeas.2005.07.028, 2006
- 440 R. Arimoto, J. L. Webb, M. Conley, Radioactive contamination of atmospheric dust over
441 Southwestern New Mexico, *Atmospheric Environ.* 2005, 39, 4745.
- 442 R.K. Chesser, M. Bondarkov, R.J. Baker, J.K. Wickliffe, B.E. Rodgers, Reconstruction of
443 radioactive plume characteristics along Chernobyl's Western trace, *J. Environ. Radioactivity*, 71,
444 147-157, doi:10.1016/S0265-931X(03)00165-6, 2004
- 445 Christoudias, T., Proestos, Y., and Lelieveld, J.: Global risk from the atmospheric dispersion of
446 radionuclides by nuclear power plant accidents in the coming decades, *Atmos. Chem. Phys.*
447 *Discuss.*, 2013, 13, 30287-30309, doi:10.5194/acpd-13-30287-2013.
- 448 Clement, C.F.; Clement, R.A.; Harrison, R.G. Charge Distributions and Coagulation of
449 Radioactive Aerosols. *J. Aerosol Sci.*, 26, 1207-1225, doi: 10.1016/0021-8502(95)00525-0, 1995
- 450 Clement, C.F.; Harrison, R.G. The Charging of Radioactive Aerosols. *J. Aerosol Sci.*, 23, 481-
451 504, doi: 10.1016/0021-8502(92)90019-R, 1992
- 452 Fuchs, N.A. *The Mechanics of Aerosols*; Pergamon Press: New York, 1964.
- 453 Gensdarmes, F.; Boulaud, D.; Renoux, A. Electrical Charging of Radioactive Aerosols—
454 Comparison of the Clement–Harrison Models with New Experiments. *J. Aerosol Sci.*, 32, 1437-
455 1458, doi: 10.1016/S0021-8502(01)00065-9, 2001
- 456 Gunn, R., Diffusion charging of atmospheric droplets by ions, and the resulting combination
457 coefficients. *J. Meteor.*, 11, 329, 339-347 doi: 10.1175/1520-
458 0469(1954)011<0339:DCOADB>2.0.CO;2, 1954



- 459 Greenfield, S. M., Ionization of radioactive particles in the free air. *J. Geophys. Res.*, 61, 27-33,
460 doi:10.1029/JZ061i001p00027, 1956
- 461 Greenfield, S. M., Rain scavenging of radioactive particulate matter from the atmosphere. *J.*
462 *Atmos. Sci.*, 14, 115-125, doi: 10.1175/1520-0469(1957)014<0115:RSORPM>2.0.CO;2, 1957
- 463 Harrison, R. G., and K. S. Carslaw (2003), Ion-aerosol-cloud processes in the lower atmosphere,
464 *Rev. Geophys.*, 41, 1012, doi:10.1029/2002RG000114, 3.
- 465 Kauppinen, E.I.; Hillamo, R.E.; Aaltonen, S.H., Sinkko, K.T.S. Radioactivity Size Distributions
466 of Ambient Aerosols in Helsinki, Finland, during May 1986 after the Chernobyl accident:
467 Preliminary Report. *Environ. Sci. Technol.*, 20, 1257-1259, doi: 10.1021/es00154a01, 1986
- 468 Kim, Y.-H., Yiacoumi, S., Lee, I., McFarlane, J., Tsouris, C., Influence of radioactivity on
469 surface charging and aggregation kinetics of particles in the atmosphere, *Environ. Sci. Technol.*,
470 48, 182-189, doi: 10.1021/es4047439 2014
- 471 Kim, Y.-H., Yiacoumi, S., Tsouris, C., Surface charge accumulation of particles containing
472 radionuclides in open air, *J. Environ. Radioactivity*, 143, 91-99, doi:
473 10.1016/j.jenvrad.2015.02.017, 2015
- 474 Kim, Y.-H., Yiacoumi, S., Nenes, A., Tsouris, C., Incorporating radioactive decay into charging
475 and coagulation of multicomponent radioactive aerosols, *J.Aer.Sci*, *in review*
- 476 Kim, Y.-H.; Yiacoumi, S.; Nenes, A.; Tsouris, C. Influence of aerosol charging on global transport
477 of radioactivity, *in preparation*
- 478 Kim, Y.-H., Yiacoumi, S., Nenes, A., Tsouris, C., Charging and coagulation of radioactive and
479 nonradioactive particles in the atmosphere. *Atmos. Chem. Phys.*, 16, 3449-3462, doi: 10.5194/acp-
480 16-3449-2016, 2016
- 481 Lee, Y.; P. Adams. A fast and efficient version of the two-moment aerosol sectional (TOMAS)
482 global aerosol microphysics model. *Aerosol. Sci. Technol.*, 46 (6), 678-689, doi:
483 10.1080/02786826.2011.643259, 2012



- 484 G. Lujanienė, V. Aninkevičius, V. Lujanas, Artificial radionucleotides in the atmosphere over
485 Lithuania, *J. Environ. Radioactivity*, 100(2), 108-119, doi:10.1016/j.jenvrad.2007.07.015, 2007
- 486 Masson, O.; Baeza, A.; Bieringer, J.; Brudecki, K.; Bucci, S.; Cappai, M.; Carvalho, F.P.; Connan,
487 O.; Cosma, C.; Dalheimer, A.; Didier, D.; Depuydt, G.; De Geer, L.E.; De Vismes, A. ; Gini, L.;
488 Groppi, F.; Gudnason, K.; Gurriaran, R.; Hainz, D.; Halldórsson, Ó.; Hammond, D.; Hanley, O.;
489 Holeý, K.; Homoki, Zs.; Ioannidou, A.; Isajenko, K.; Jankovic, M.; Katzlberger, C.; Kettunen, M.;
490 Kierepko, R.; Kontro, R.; Kwakman, P.J.M.; Lecomte, M.; Vintro, L.L.; Leppänen, A.-P.; Lind,
491 B.; Lujanienė, G. ; Ginnity, P.M.; Mahon, C. M.; Malá, H.; Manenti, S. ; Manolopoulou, M.;
492 Mattila, A.; Muring, A.; Mietelski, J.W.; Møller, B.; Nielsen, S.P. ; Nikolic, J.; Overwater,
493 R.M.W.; Pálsson, S. E.; Papastefanou, C.; Penev, I.; Pham, M.K.; Povinec, P.P.; Ramebäck, H.;
494 Reis, M.C.; Ringer, W.; Rodriguez, A.; Rulík, P.; Saey, P.R.J.; Samsonov, V.; Schlosser, C.;
495 Sgorbati, G.; Silobritiene, B.V.; Söderström, C.; Sogni, R.; Solier, L.; Sonck, M.; Steinhauser, G.;
496 Steinkopff, T.; Steinmann, P.; Stoulos, S.; Sýkora, I.; Todorovic, D.; Tooloutalaie, N.; Tositti, L.;
497 Tschiersch, J.; Ugron, A.; Vagena, E.; Vargas, A.; Wershofen, H.; Zhukova, O. Tracking of
498 Airborne Radionuclides from the Damaged Fukushima Dai-Ichi Nuclear Reactors by European
499 Networks. *Environ. Sci. Technol.*, 45, 7670-7677, doi: 10.1021/es2017158, 2011
- 500 J.P. McBride, R.E. Moore, J.P. Witherspoon, R.E. Blanco, Radiological impact of airborne
501 effluents of coal and nuclear-plants, *Science*, 202, 4372, 1045-1050 doi:
502 10.1126/science.202.4372.1045, 1978
- 503 Mohnen, V. A., Formation, Nature, and Mobility of Ions of Atmospheric Importance, in *Electrical*
504 *Processes in Atmospheres*, H. Dolezalek, R. Reiter, and H. Landsberg, eds., Steinkopff, Darmstadt,
505 Germany, pp. 1–17, doi: 10.1007/978-3-642-85294-7_1, 1976
- 506 Mulpuru, S.R.; Pellow, M.D.; Cox, D.S.; Hunt, C.E.L.; Barrand, R.D. Characteristics of
507 Radioactive Aerosols Generated from a Hot Nuclear Fuel Sample. *J. Aerosol Sci.*, 23, S827-S830,
508 doi: 10.1016/0021-8502(92)90539-8, 1992
- 509 H. Ooe, R. Seki, N. Ikeda, Particle-size distribution of fission products in airborne dust collected
510 at Tsukuba from April to June 1986., *J. Environ. Radioactivity*, 6(3), 219-223, doi: 10.1016/0265-
511 931x(88)90078-1, 1988



- 512 Seinfeld, J.H., Pandis, S.N., Atmospheric Chemistry and Physics: From Air Pollution to Climate
513 Changes. Wiley, New York, USA ISBN: 0-471-17815-2, 2006
- 514 Simons, S. The Coagulation and Deposition of Radioactive Aerosols. *Ann. Nucl. Energy*, 8, 287-
515 294, doi: 10.1016/0306-4549(81)90094-3, 1981
- 516 Spielman, L. A., Viscous interactions in Brownian coagulation, *J. Colloid Interface Sci.* 33, 562
517 doi: 10.1016/0021-9797(70)90008-1, 1970
- 518 Sow, M., Lemaitre, P., Influence of electric charges on the washout efficiency of atmospheric
519 aerosols by raindrops. *Ann. Nucl. Energy*, 93, 107-113, doi:10.1016/j.anucene.2015.12.036, 2016
- 520 Tripathi, S., Harrison R. G., Scavenging of electrified radioactive aerosol. *Atmos. Environ.*, 35,
521 5817-5821, doi:10.1016/S1352-2310(01)00299-0, 2001
- 522 Tzivion, S.; Feingold, G.; Levin, Z. An Efficient Numerical Solution to the Stochastic Collection
523 Equation. *J. Atmos. Sci.*, 44, 3139-3149, doi: 10.1175/1520-
524 0469(1987)044<3139:AENSTT>2.0.CO;2, 1987
- 525 V. I. Yoshenko, V. A. Kashparov, V. P. Protsak, S. M. Lundin, S. E. Levchuk, A. M. Kadygrib, S.
526 I. Zvarich, X. V. Khomutinin, I. M. Maloshtan, V. P. Lanshin, M. V. Kovtun, J. Tschiersch,
527 Resuspension and redistribution of radionucleotides during grassland and forest fires in the
528 Chernobyl exclusion zone. Part I: fire experiments, *J. Environ. Radioactivity*, 86 (2), 143-163, doi:
529 10.1016/j.jenvrad.2005.08.003, 2006
- 530 V. I. Yoshenko, V. A. Kashparov, S. E. Levchuk, A. S. Glukhovskiy, Y. V. Khomutni, V. P.
531 Protsak, S. M. Lundin, J. Tschiersch, Resuspension and redistribution of radionucleotides during
532 grassland and forest fires in the Chernobyl exclusion zone. Part II: modeling the transport
533 process, *J. Environ. Rad.*, 87, 260-278, doi: 10.1016/j.jenvrad.2005.08.003, 2006
- 534 Yoshida, N.; Kanda, J. Tracking the Fukushima Radionuclides. *Science*, 336, 1115-1116, doi:
535 10.1126/science.1219493, 2012



Table 1. General simulation conditions

Parameter	Iodine	Cs	Reference
Specific radioactive decay [Bq μm^{-3}]	43800	64	Clement et al., 1992, 1995
The number of ion pairs produced per decay	1945	2067	Kim et al., 2015
Minimum height [m]	200	200	TOMAS default settings
Maximum height [m]	1000	1000	
# Height levels	5	5	
Temperature [K]	293	293	Atmospheric conditions

Table 2 - Parameter space for sensitivity analysis

Parameter	Range	Notes
Geometric mean diameter (D_g)	30 nm – 5.2 μm	Range of atmospherically relevant sizes
Initial #concentration (Particles m^{-3})	10^6 - 10^{13}	Range of atmospherically relevant concentrations
Standard geometric deviation (SGD)	1.5-3.0	Range of atmospherically relevant deviations
Mobility ratio (X)	0.7-1	From Mohnen, 1976 & Kim et al., 2014

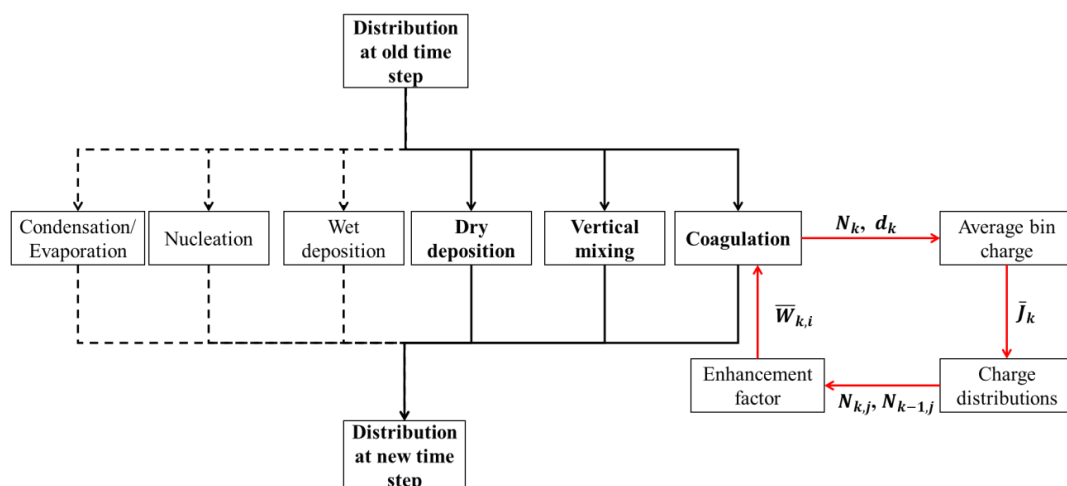


Figure 1. Flow diagram of the computational scheme in TOMAS-RC. The number concentration and diameter of each bin are passed from the coagulation subroutine to the aerosol charging subroutine, where the average charge and charge distributions are calculated, and then used to estimate the enhancement factor, which is returned to the TOMAS coagulation module. Processes in bold are the ones active in TOMAS-RC.

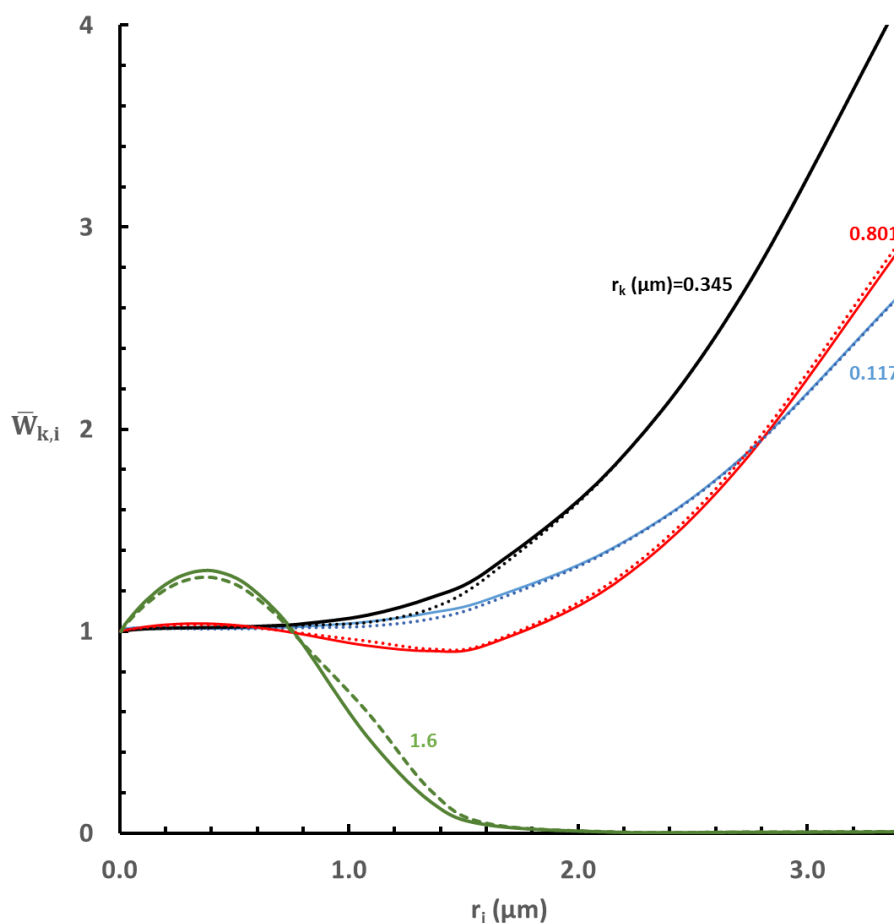


Figure 2. Enhancement factors ($\bar{W}_{k,i}$) predicted using TOMAS with the accelerated computation scheme described in section 2.3 (dashed lines) versus the full resolution computations (solid lines) between particles of size r_k and r_i . For fine particles, the enhancement factor increases dramatically with increasing particle size, while for coarser aerosol, it reaches a maximum and then decays to almost 0. The r_i values chosen were the closest that the TOMAS bins describe, to the ones used in Clement (1995).

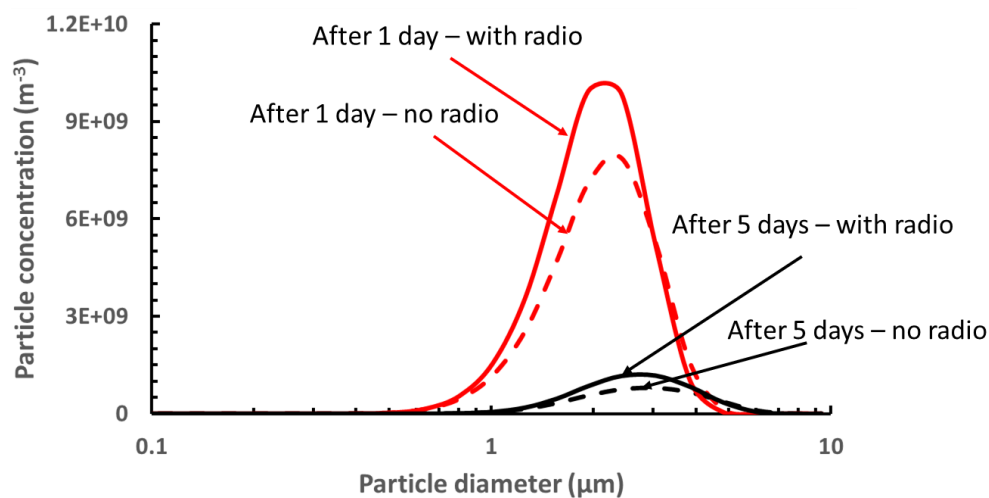


Figure 3. Evolution of the size distribution of ^{137}Cs aerosols at 400 m ($X=0.7$, $t = 5$ days, $d_g = 1.5 \mu\text{m}$, $\sigma_g = 1.5$, and $N_t = 10^{11} \text{m}^{-3}$). Shown are results with radioactive decay (solid lines) and without radioactive decay (dashed lines).

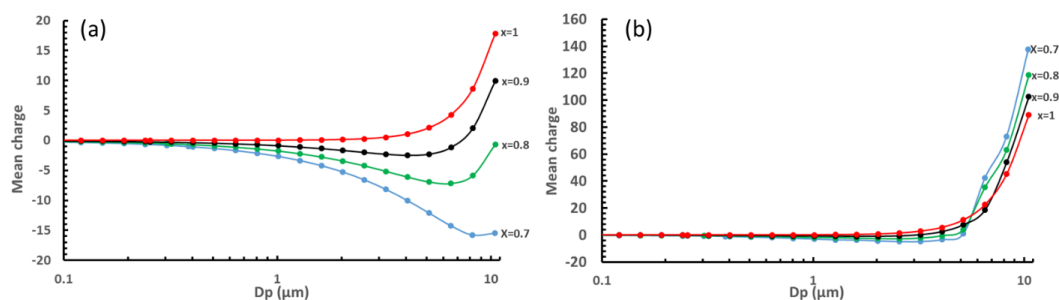


Figure 4. Mean charge values for particle sizes between 0.1 and 10 μm , for ^{137}Cs (a) and ^{131}I (b), for X values of 0.7, 0.8, 0.9 and 1. For the case of ^{137}Cs , the average charge is negative for all size bins when $0.7 \leq X \leq 0.8$, leading to inhibition of coagulation for all size bins. For $X=0.9$, the mean charge is negative for all particles below 3 μm , but become positive for larger sizes, leading to inhibition of coagulation between particles of small sizes, and enhancement between particles below and above that threshold. ^{131}I exhibits similar behavior, but because of its much higher decay rate, particles tend to accumulate much smaller negative charges and significantly larger positive ones. For $0.7 \leq X \leq 0.8$, particles up to 4 μm accumulate a small amount of negative charge, while, above that size cutoff all particles are strongly positively charged, implying accelerated coagulation rates between particles belonging to the different sides of the cutoff and inhibition for ones belonging on the same. Larger X leads to the entire size spectrum being positively charged and inhibition across all particle sizes.

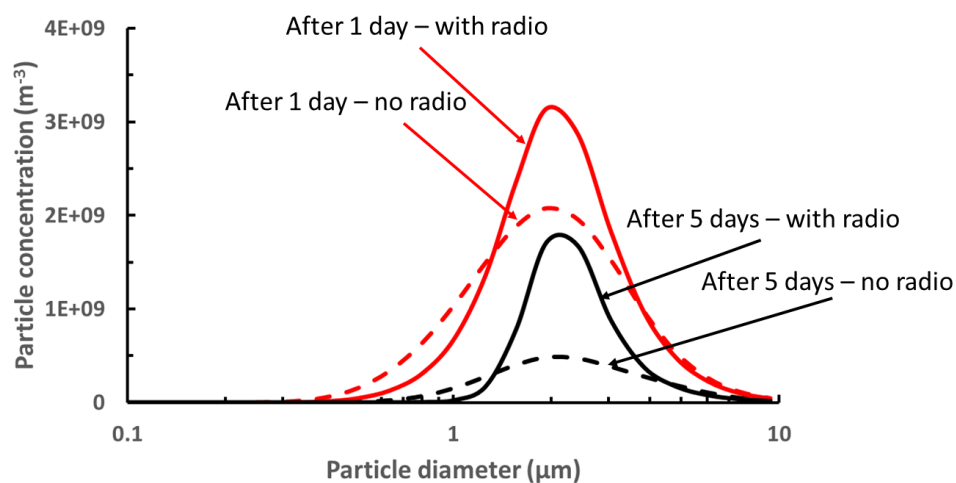


Figure 5. Evolution of the size distribution of ^{131}I aerosols at 400 m ($X=0.7$, $t = 5$ days, $d_g = 1.5$ μm , $\sigma_g = 2.5$, and $N_t = 10^{10} \text{ m}^{-3}$). Shown are results with radioactive decay (solid lines) and without radioactive decay (dashed lines).

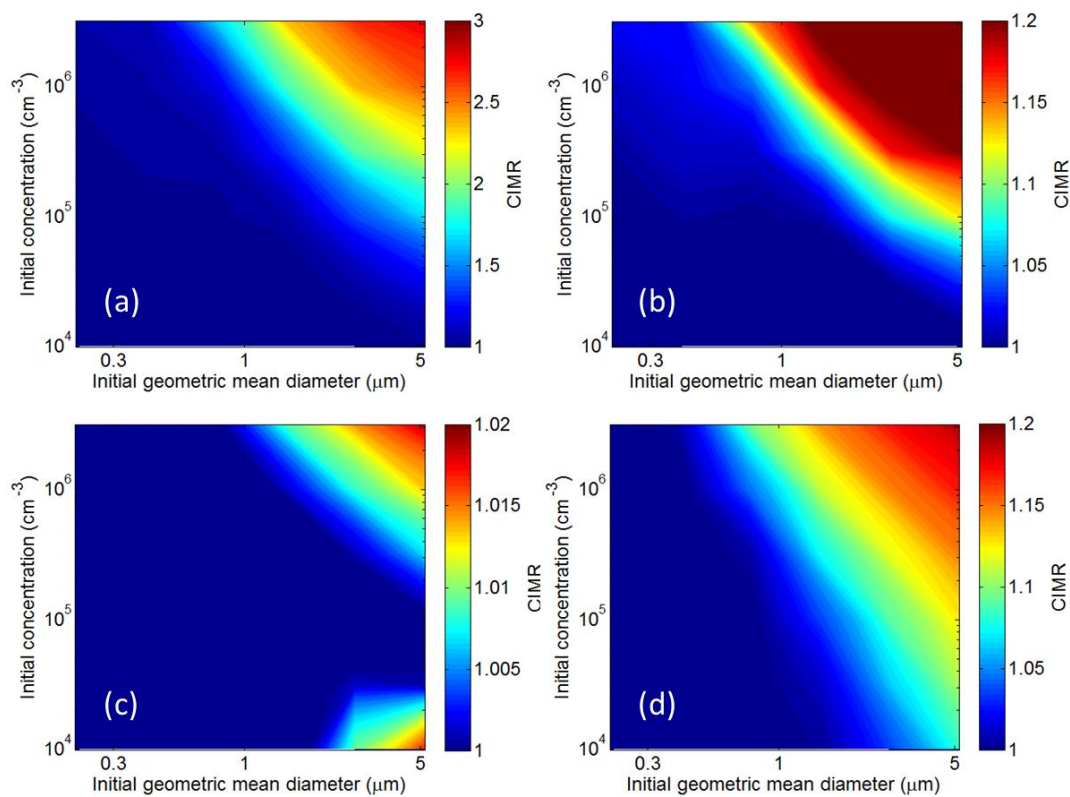


Figure 6. CIMR for ^{137}Cs aerosols after 5 days for X values of (a) 0.7, (b) 0.8, (c) 0.9 and (d) 1; $\sigma_g = 2.0$.

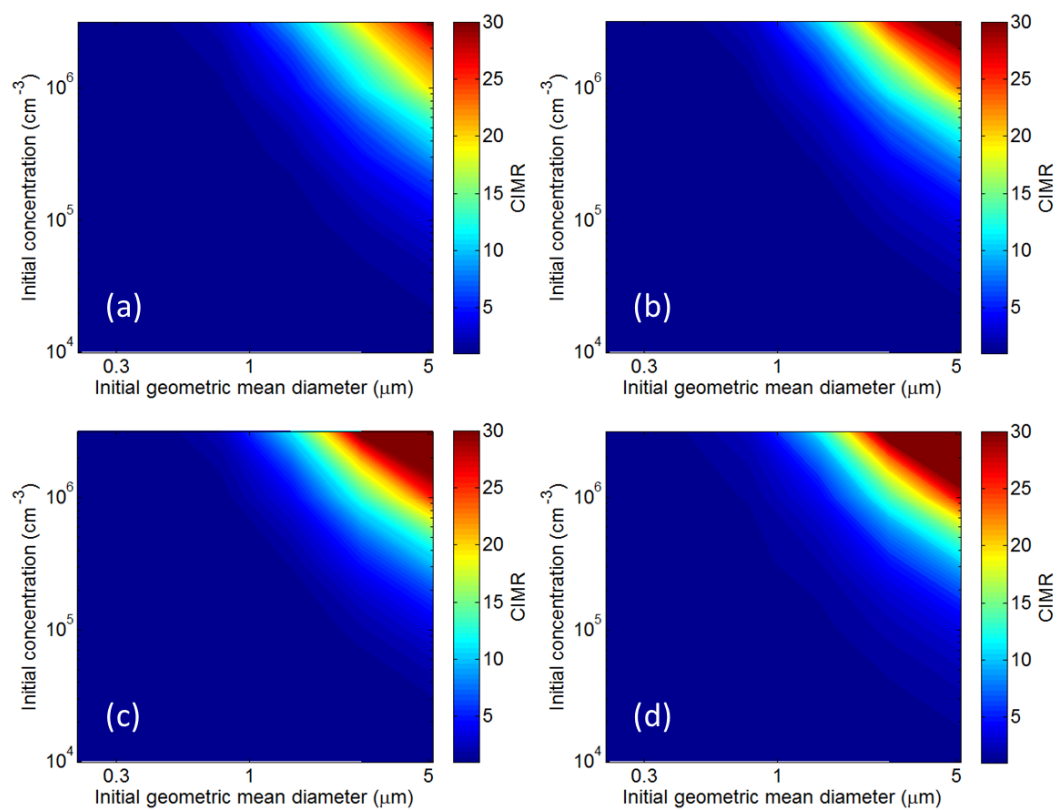


Figure 7. CIMR for ^{131}I particles after 5 days for X values of (a) 0.7, (b) 0.8, (c) 0.9 and (d) 1; $\sigma_g = 2.0$.

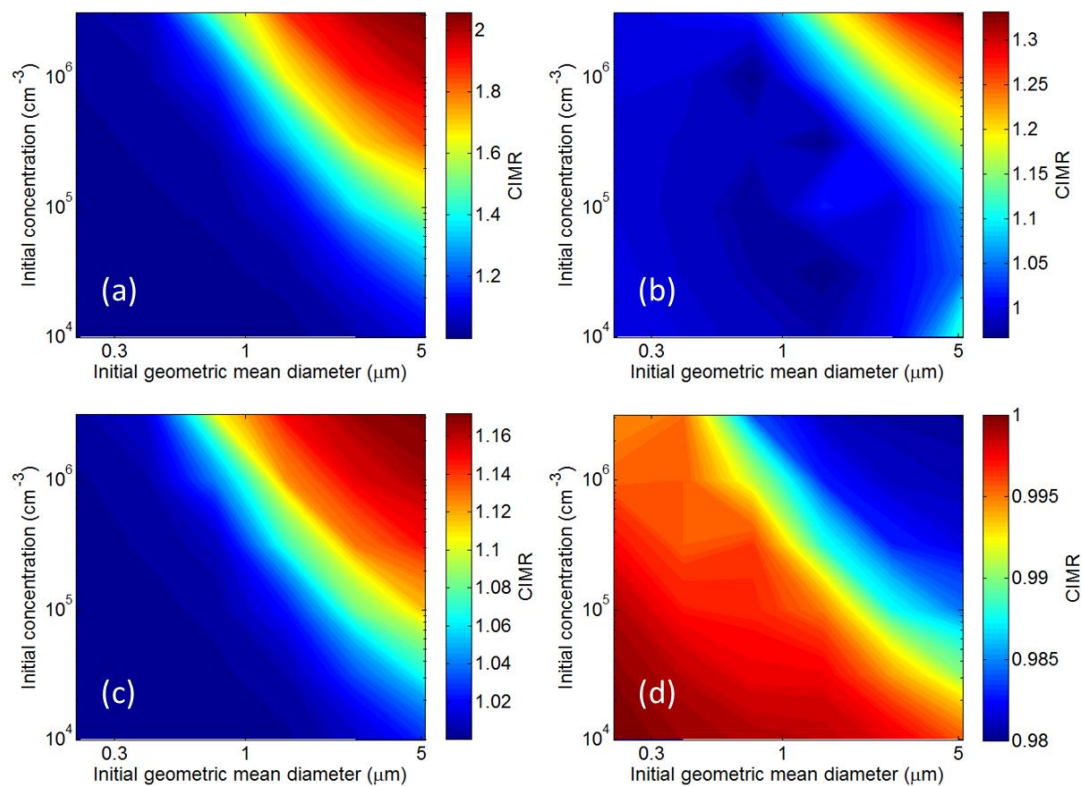


Figure 8. CIMR for particles under diffusion charging conditions, after 5 days for X values of (a) 0.7, (b) 0.8, (c) 0.9 and (d) 1; $\sigma_g = 2.0$.